RSC Advances

PAPER

View Article Online
View Journal | View Issue

Cite this: *RSC Adv.*, 2021, **11**, 22125

Synthesis of macroscopic monolithic metal–organic gels for ultra-fast destruction of chemical warfare agents†

Chuan Zhou, [ab] Shouxin Zhang, [ab] Hongjie Pan,[b] Guang Yang,[b] Lingyun Wang,[b] Cheng-an Tao [c] and Heguo Li*[b]

The potential threat that has originated from chemical warfare agents (CWAs) has promoted the development of advanced materials to enhance the protection of civilian and military personnel. Zr-based metal–organic frameworks (Zr-MOFs) have recently been demonstrated as excellent catalysts for decomposing CWAs, but challenges of integrating the microcrystalline powders of Zr-MOFs into monoliths still remain. Herein, we report hierarchically porous monolithic UiO-66-X xerogels for the destruction of CWAs. We found that the UiO-66-NH_2 xerogel with a larger pore size and a higher surface area than the UiO-66-NH_2 powder possessed better degradability of 2-chloroethyl ethyl sulfide (2-CEES), which is a sulfur mustard simulant. These UiO-66-X xerogels exhibit outstanding performance for decomposing CWAs. The half-lives of vesicant agent sulfur mustard (HD) and nerve agent *O*-ethyl *S*-[2-(diisopropylamino)ethyl] methylphosphonothioate (VX) are as short as 14.4 min and 1.5 min, respectively. This work is, to the best of our knowledge, the first report on macroscopic monolithic UiO-66-X xerogels for ultrafast decomposition of CWAs.

Received 4th March 2021
Accepted 20th May 2021

DOI: 10.1039/d1ra01703a

rsc.li/rsc-advances

1. Introduction

Chemical warfare agents (CWAs) such as sulfur mustard (HD) and VX are lethal chemicals that pose an extreme risk to national security and public health, due to occasional or deliberate emissions.[1] Detoxification of CWAs is an increasing research field that has generated great interest from the scientific and industrial communities. Current state-of-the-art materials for the capture of CWAs mainly rely on impregnated active carbons, which suffer from problems such as slow degradation kinetics, low capacity, and/or a lack of tailorability.[2] Thus, there is an urgent need to explore novel self-detoxifying materials to efficiently protect civilian and military personnel.

Recently, resourceful studies have been carried out on the catalytic performance of the decontamination of CWAs. Among them, metal–organic frameworks (MOFs) that are assembled by metal ions or clusters with organic linkers through coordination bonds have been extensively studied and have shown intriguing performances in CWA removal, due to their exceptionally large surface area, high porosity, tunable textural and chemical properties, and their abundant catalytic sites.[3–5] In particular, Zr-based metal–organic frameworks (Zr-MOFs) have attracted great research attention as potential heterogeneous catalysts, due to their easy and numerous synthetic methods,[6] and their exceptionally high thermal, chemical and mechanical stabilities.[7] Meanwhile, it has been demonstrated that Zr-MOFs such as MOF-808, PCN-777, NU-1000 and UiO-66-NH_2 have unprecedented catalytic degradation rates for nerve agents with half-lives of less than 0.5 min.[8–10] However, the crystallization of Zr-MOFs often leads to microcrystalline powders. The application of Zr-MOF powders is greatly hampered, due to their inherent problems such as particle aggregation, poor processability and handling, mass transfer limitations, and significant pressure drop in an adsorption bed.[11–15] To overcome the issues of Zr-MOF powders, many methods have been reported to construct Zr-MOF macroscale structures by either integrating Zr-MOFs into support materials such as fibers,[16–18] polymeric monoliths[19,20] and foams,[21–23] or pelletizing Zr-MOF powders *via* mechanical compression or extrusion.[24–26] However, both strategies still have issues such as reduced adsorption capacities, due to the use of Zr-MOF as a secondary component, and pressure-induced losses of crystallinity and porosity. Therefore, the development of pure monolithic Zr-MOFs has become a novel research field in recent years.

Metal–organic gels (MOGs) linked by metal–ligand coordination associated with hydrogen bonding, hydrophobic effects, π–π stacking and van der Waals interactions are a class of fabricable, hierarchically porous, pure MOF materials.[27,28] Preparation of MOGs mainly depends on mismatched growth of

[a]*State Key Laboratory of NBC Protection for Civilians, Beijing 102205, PR China*
[b]*Research Institute of Chemical Defense, Beijing 102205, PR China*
[c]*College of Liberal Arts and Science, National University of Defense Technology, Changsha 410073, China*

† Electronic supplementary information (ESI) available. See DOI: 10.1039/d1ra01703a

the MOF particles by regulating key factors such as synthesis temperature and time,[27] reactant concentration,[11] organic-linker functionality and solvent[29] in the gelation process. Therefore, the combination of Zr-MOFs with a suitable gelation process could shed light on Zr-MOF applications in the detoxification of CWAs. Up to now, only sporadic examples involving Zr-based metal–organic gels (Zr-MOGs) have been reported. For example, the synthesis of Zr-MOGs from $ZrCl_4$ in a mixture of solvent/water proceeds through a rapid method at room temperature.[29] Bueken *et al.* described a series of Zr-MOGs synthesized in DMF using $ZrOCl_2 \cdot 8H_2O$ as a precursor and a mixture of HCl/AA as a modulator.[11] However, there has been almost no systematic or detailed investigation on the post-treatment of gel synthesis.

In this contribution, we systematically investigate the effect that post-treatment conditions have on porosity for the optimization and preparation of macroscopic monolithic UiO-66-X xerogels (UiO-66 and UiO-66-NH_2 xerogels). As far as we know, no report regarding UiO-66-X xerogels for the catalytic destruction of real CWAs has appeared in the literature. Herein, we have first investigated the catalytic degradation performance of the UiO-66-NH_2 xerogel and the UiO-66-NH_2 powder for use with 2-chloroethyl ethyl sulfide (2-CEES), which is a sulfur mustard simulant. Then, we attempted to identify the sulfur mustard (HD) and VX decomposition abilities of neat UiO-66-X xerogels at room temperature. This is also the first demonstration of ultra-fast destruction of CWAs using Zr-MOFs xerogels.

2. Materials and methods

2.1. Chemicals and characterization methods

Unless otherwise noted, ACS reagent grade chemicals and solvents were purchased from commercial vendors and were used without further purification. Terephthalic acid (H_2BDC), 2-aminoterephthalic acid (H_2N-BDC), zirconyl chloride octahydrate ($ZrOCl_2 \cdot 8H_2O$) and 2-chloroethyl ethyl sulfide (2-CEES) were obtained from Shanghai Macklin Biochemical Co., Ltd. Methanol, alcohol, acetone, *N*,*N*-dimethylformamide (DMF), hydrochloric acid (37%) and acetic acid were obtained from Shanghai Aladdin Chemicals Co., Ltd.

Powder X-ray diffraction (PXRD) data were collected at room temperature on a Bruker D2 Phaser diffractometer, with Cu K-alpha radiation (λ = 1.54178 Å). Thermogravimetric analysis (TGA) was performed in air using a Mettler TGA/DSC 1 instrument equipped with an alumina crucible and heated at a rate of 5 °C min^{-1} up to 800 °C. N_2 physisorption measurements were measured at 77 K on a micromeritics ASAP 2020 instrument. Prior to the measurements, the samples (20–40 mg) were degassed for 8 h at 110 °C and under 0.1 mbar vacuum. Transmission electron microscopy (TEM) was performed on a JEM-2100 microscope, operated in scanning mode (accelerating voltage of 200 kV). Scanning electron microscope (SEM) images were recorded on a JEOL JSM-IT300 microscope and were processed using the ImageJ software. Inductively coupled plasma-optical emission spectroscopy (ICP-OES) and C, H and N elemental analyses were carried out using a Leeman Prodigy 7 ICP-OES analyser and a Vario EL elemental analyser, respectively.

2.2. Synthesis of the UiO-66 xerogel

The UiO-66 xerogel was prepared under optimum conditions by dissolving H_2BDC (5 mmol) and $ZrOCl_2 \cdot 8H_2O$ (7.25 mmol) in DMF (30 mL) under sonication for 15 min. Afterwards, HCl (1.5 mL) and acetic acid (2.0 mL) as modulators were added to the above solution, and the mixture was left for 5 min under sonication. The resulting homogeneous solution was then allowed to stand at 373 K for 2 h in a closed container to yield a thick white UiO-66 gel. Subsequently, fresh DMF was added to the above UiO-66 gel and was mixed well. The diluted gel suspension was centrifuged (5000 rpm, 5 min) and the supernatant was decanted. The gel was then washed three times with ethanol and dried in air at 30 °C. The obtained xerogel was immersed in acetone and methanol for 12 h and dried in air at 30 °C to produce the macroscopic monolithic UiO-66 xerogel, as shown in Fig. 1.

2.3. Synthesis of the UiO-66-NH_2 xerogel

The UiO-66-NH_2 xerogel was prepared by replacing H_2BDC in the UiO-66 xerogel synthesis procedure with an equimolar amount of H_2N-BDC.

2.4. Synthesis of the UiO-66-NH_2 powder[33]

$ZrOCl_2 \cdot 8H_2O$ (0.54 mmol), H_2N-BDC (0.75 mmol), 1 mL of HCl and 15 mL of DMF were added into a 100 mL Pyrex Schott bottle before being sonicated for 10 min until fully dissolved. The Pyrex Schott bottle was sealed and heated to 80 °C for 12 h. The resulting pale yellow solid was centrifuged and washed three

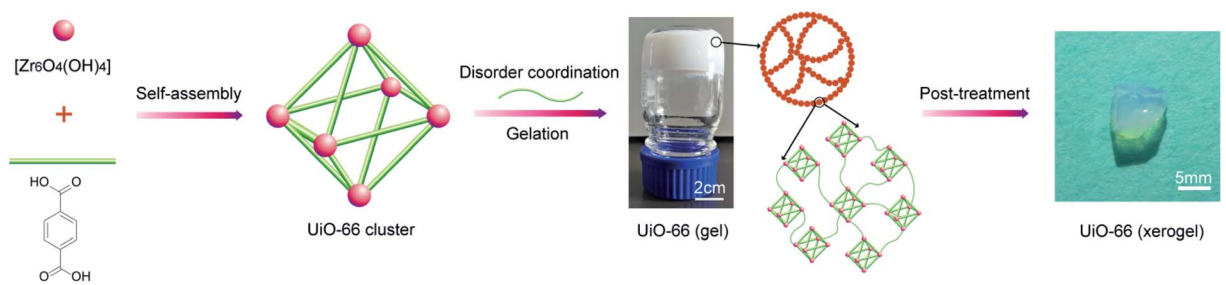

Fig. 1 Schematic of the synthesis of the UiO-66 xerogel.

times with DMF and alcohol. The sample was activated for 8 h in a vacuum oven at 110 °C.

2.5. Degradation experiments

Important! *CWAs (HD, VX) are known to be lethal if inhaled or in contact with skin. Experiments should be performed under/by trained personnel in adequate facilities.*

The catalytic degradation of 2-CEES, HD and VX was evaluated. The degradation of 2-CEES and HD was carried out by extraction: 25 μL $CHCl_3$ solution containing 2.5 μL 2-CEES or HD was added to 25 mg xerogel in each glass vial, which were vortexed and left standing for various periods of time before extracting with 3 mL ethanol for 3 times and analyzing for residual 2-CEES or HD by GC-MS. 20 μL Pentane solution containing 0.4 μL VX was added to 20 mg xerogel in each glass vial. Afterwards, the vials containing the reaction mixtures were vortexed and were left standing at room temperature. Each vial was taken out for analysis at regular times. The residual VX was extracted in 2 mL of acetonitrile and the solution was subjected to gas chromatography with an FID detector.

3. Results and discussion

3.1. Xerogel optimization

Based on the essential principle of optimising the porosity of the xerogel, we selected UiO-66 as a prototype to perform

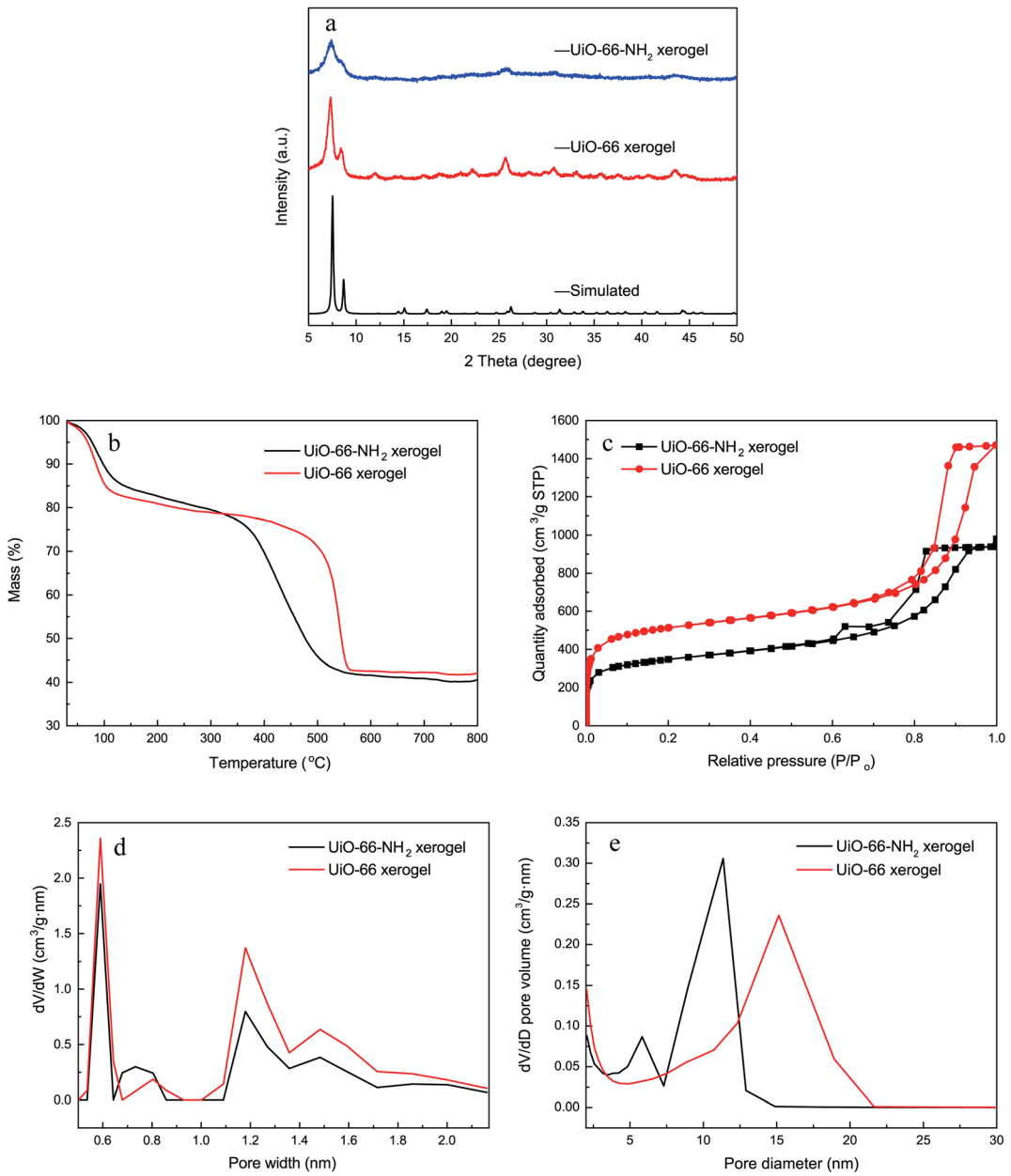

Fig. 2 Characterization of the xerogels. (a) XRD patterns; (b) TGA curves; (c) N_2 adsorption–desorption isotherms; (d) NLDFT pore size distributions; (e) BJH pore size distributions.

a screening of several post-treatment parameters such as drying temperature, washing procedure, centrifugation procedure and metal-to-ligand ratio, in order to determine their influence on the porosity of the xerogel (Table S1†). Tian *et al.* noted that a low temperature of drying is beneficial for the formation of the monolithic HKUST-1 gel.[12] Subsequently, we investigated the effect of drying temperature on the porosity of the UiO-66 xerogel. The result showed that the Brunauer–Emmett–Teller surface area (S_{BET}) and the total pore volume (V_{tot}) of the xerogel could be enhanced by appropriately increasing the drying temperature (Table S1,† #1–#3). This may be due to the more rapid solvent evaporation rate at a higher temperature, resulting in an increase in mesoporous content in the xerogel. We further evaluated the influence of the washing procedure (washing solvents and washing times) on the porosity of the UiO-66 xerogel by washing the gel before drying at 30 °C. The result showed that the use of ethanol instead of DMF to wash the UiO-66 gel helps to enhance the S_{BET} and V_{tot} values of the xerogel (Table S1,† #1 *vs.* #5, #4 *vs.* #6). In addition, we found that S_{BET} and V_{tot} of the xerogel could be significantly increased by increasing the number of ethanol washing times (Table S1,† #5 *vs.* #6), whereas the number of DMF washing times had little significant effect (Table S1,† #1 *vs.* #4). Furthermore, we examined the effect of centrifugation time and found that a prolonged centrifugation time had no significant effect on the porosity of the xerogel (Table S1,† #1 *vs.* #7). A defect density would also greatly affect the porosity of the material.[30,31] Finally, a series of UiO-66 xerogels (Table S1,† UiO-66-G, UiO-66-H, UiO-66-I) were synthesized by modulating different metal-to-ligand ratios, and these were characterized by TGA. All the synthesized samples exhibited excellent thermal stability in air up to 500 °C. The numbers of BDC linker in each unit of synthesized UiO-66 xerogel could be calculated according to the amount of mass lost (%) between 300 °C and 600 °C.[32] The mass loss (%) of the BDC linkers for UiO-66-G, UiO-66-H and UiO-66-I was 40.6%, 40.3% and 37.5%, respectively (Fig. S1†). The calculated BDC ligands per unit of UiO-66-G, UiO-66-H and UiO-66-I were 4.5, 4.4 and 4.1, respectively. Less BDC ligands means more missing-linker defects, indicating that more defects exist in the structural units of UiO-66-I, and this results in a higher specific surface area and pore volume.

3.2. Structural and morphological characterizations

Fig. 2a shows the XRD patterns of the monolithic UiO-66 xerogel and the UiO-66-NH_2 xerogel. The apparent peaks at around 7° and 8.5° correspond well with the (111) and (200) reflections of the UiO-66 structure.[33] Furthermore, broad diffraction peaks primarily originate from Scherrer broadening and nanoparticles. The morphologies of the monolithic UiO-66 xerogel and the UiO-66-NH_2 xerogel are characterized by SEM and TEM. The SEM images show a rough surface with closely packed nanoparticles, as seen in Fig. 3e–h. The TEM results further confirm that the monolith consists of compact nanoparticles with particle interstitial space (Fig. 3a–d). Elemental analysis shows that the experimental compositions of the UiO-66-X xerogels are significantly different from their theoretical compositions (Table S2†), indicating the presence of defects, as illustrated by the lower experimentally observed carbon and nitrogen content relative to the theoretical content. In addition, the increase in hydrogen content of the experimental samples may indicate the existence of water in the crystal structure. The TGA curve of the monolithic UiO-66-X xerogels is illustrated in Fig. 2b. The high thermal stability of the monolith is consistent with the previously reported literature.[34] As shown in Fig. 2c, the N_2 adsorption–desorption isotherms are of Type IV, and this confirms the existence of a micro–mesoporous structure of the monolithic UiO-66 xerogel and of the UiO-66-NH_2 xerogel. The Brunauer–Emmett–Teller surface areas (S_{BET}), micro pore volumes (W_o) and total pore volumes (V_{tot}) are shown in Table

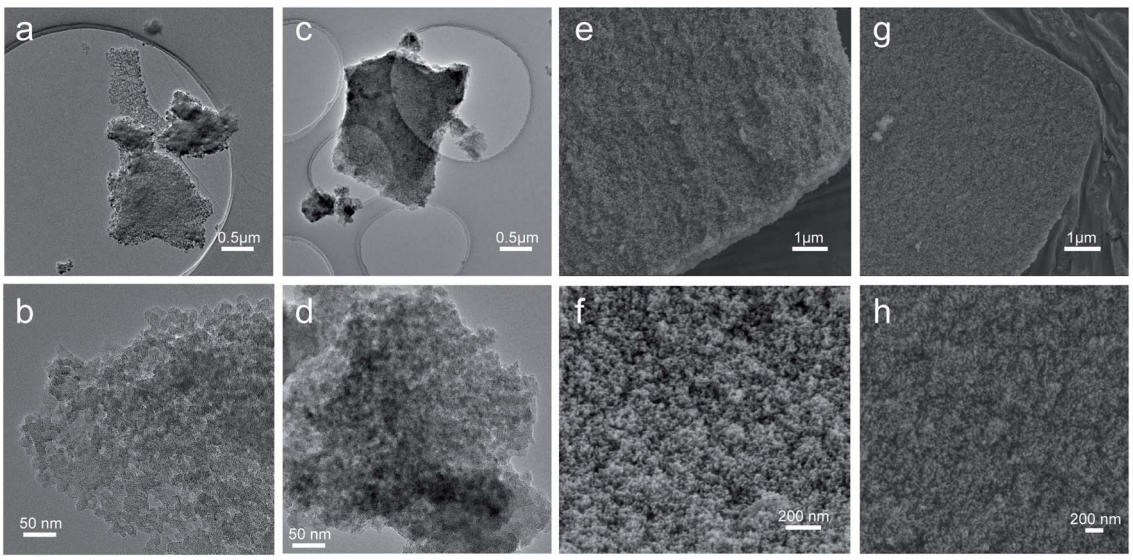

Fig. 3 Electron microscopy (top: low magnification; down: high magnification) images for the UiO-66-X xerogels. TEM images of the UiO-66 xerogel (a and b) and UiO-66-NH_2 xerogel (c and d); SEM images of the UiO-66 xerogel (e and f) and UiO-66-NH_2 (g and h) xerogel.

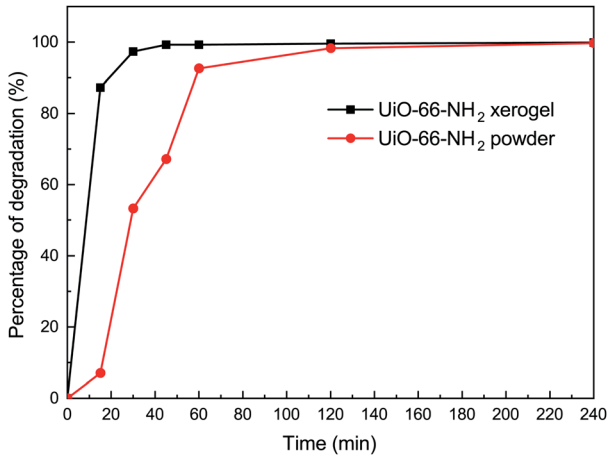

Fig. 4 Degradation of 2-CEES on the UiO-66-NH_2 xerogel and on the UiO-66-NH_2 powder.

S3.† Interestingly, these experimental values are higher than the theoretical maxima, and this may be related to the presence of extensive mesoporosity in the xerogels. The NLDFT analysis confirms the microporosity (Fig. 2d), while the BJH pore size distribution significantly highlights the extensive mesoporosity of between 5 and 20 nm (Fig. 2e). The mesoporosity of the xerogels is not generated by crystalline defects, but corresponds to interparticle voids.

3.3. Degradation properties

In order to understand the effect of state on the decomposition of CWAs, a decomposition experiment for 2-CEES was implemented at room temperature. Data for the structural characterization of the UiO-66-NH_2 powder are given in Fig. S2.† Fig. 4 shows the decomposition rates of 2-CEES over time on the UiO-66-NH_2 xerogel and UiO-66-NH_2 powder. The UiO-66-NH_2 xerogel exhibits a faster reaction rate, with a half-life of 8.2 min, than the UiO-66-NH_2 powder that exhibits a $t_{1/2}$ value of 29 min. This finding can be attributed to the larger pore size and higher surface area of the UiO-66-NH_2 xerogel, allowing for 2-CEES molecules to diffuse more rapidly and/or access more active sites.

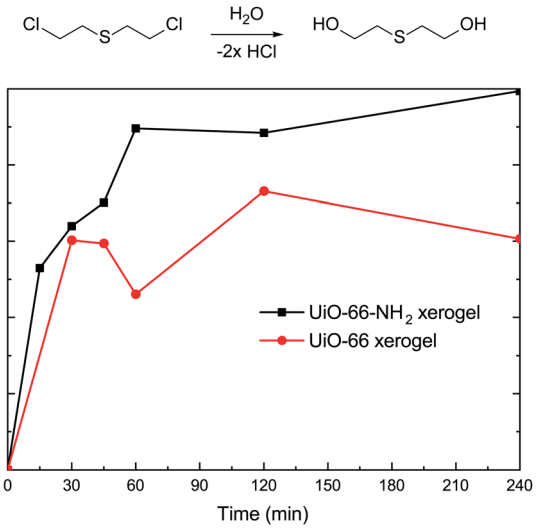

Fig. 5 Degradation of HD on the UiO-66 xerogel and on the UiO-66-NH_2 xerogel.

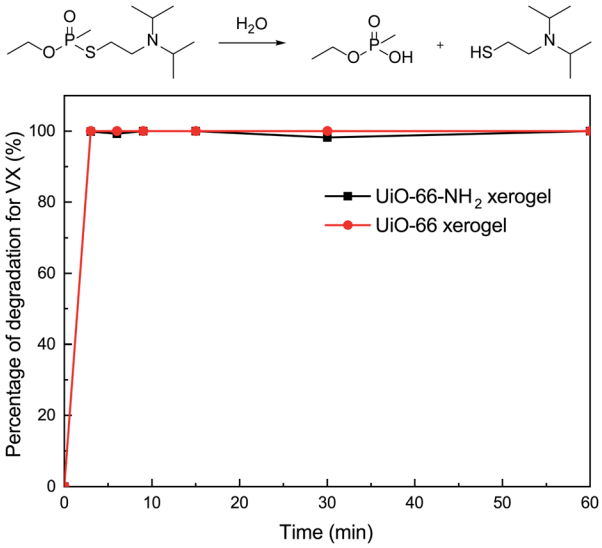

Fig. 6 Degradation of VX on the UiO-66 xerogel and on the UiO-66-NH_2 xerogel.

In addition to the simulant 2-CEES, we further tested our monolithic UiO-66-X xerogels on the hydrolytic degradation of HD, a real CWA (Fig. 5). As is well-known, Zr-based metal–organic frameworks (Zr-MOFs) are highly active in the decomposition of P–X bonds (X = F, Cl, S, O) of nerve agents, but they are poorly active in the destruction of C–Cl of vesicant agents. This limits the practical application of Zr-MOFs for the degradation of unknown chemical threats. In this regard, we have found that the incorporation of an amino-group leads to significant improvement of the degradation of C–Cl bonds found in HD. For the UiO-66-NH_2 xerogel, we observed 100% HD conversion in 240 min of reaction. The UiO-66-NH_2 xerogel ($t_{1/2}$ = 14.4 min) shows a faster destruction rate compared to the pristine UiO-66 xerogel ($t_{1/2}$ = 24.8 min).

To further investigate the catalytic performance of our materials, we also evaluated the behavior of the xerogels for the hydrolytic degradation of nerve agent VX. In this regard, it should be noted that both of the xerogels exhibited rapid VX degradation ($t_{1/2} \leq 1.5$ min) and 100% conversion within 3 min (Fig. 6). There was little difference in the VX decomposing ability for the UiO-66 and UiO-66-NH_2 xerogels. This discovery is in accordance with the previous report of Ryu *et al.*[10] who studied the detoxification of GD on UiO-66 and UiO-66-NH_2 powders.

4. Conclusions

In summary, UiO-66-X xerogels have been prepared and studied for the degradation of CWAs. The results indicate that the UiO-

66-NH_2 xerogel ($t_{1/2}$ = 8.2 min) displays excellent catalytic performance for the degradation of 2-CEES compared to the UiO-66-NH_2 powder ($t_{1/2}$ = 29 min). Using these UiO-66-X xerogels shortens the half-lives of HD and VX to 14.4 min and 1.5 min, respectively. We also confirmed that there is little obvious degradability difference between the UiO-66 and UiO-66-NH_2 xerogels for nerve agents in actual situations. This contribution shows that Zr-MOFs xerogels have remarkable prospects for use in future CWA protective applications.

Conflicts of interest

There are no conflicts to declare.

Acknowledgements

This work was financially supported by the State Key Laboratory of NBC Protection for Civilian Foundation of China (SKLNBC201807) and by the National Natural Science Foundation of China (No. 22075319). The authors also acknowledge the Analytical Instrumentation Center of Peking University.

References

1 M. Zhang, Y. Liu, J. Chen, H. Liu, X. Lu, J. Wu, Y. Zhang, Y. Lin, Q. Liu, H. Wang, L. Guo, R. Gao, B. Xu and J. Xie, *Anal. Chem.*, 2020, **92**, 10578–10587.
2 S. S. Mondal and H. J. Holdt, *Angew. Chem., Int. Ed.*, 2016, **55**, 42–44.
3 J. B. DeCoste and G. W. Peterson, *Chem. Rev.*, 2014, **114**, 5695–5727.
4 I. Stassen, B. Bueken, H. Reinsch, J. F. M. Oudenhoven, D. Wouters, J. Hajek, V. Van Speybroeck, N. Stock, P. M. Vereecken, R. Van Schaijk, D. De Vos and R. Ameloot, *Chem. Sci.*, 2016, **7**, 5827–5832.
5 T. Islamoglu, Z. Chen, M. C. Wasson, C. T. Buru, K. O. Kirlikovali, U. Afrin, M. R. Mian and O. K. Farha, *Chem. Rev.*, 2020, **120**, 8130–8160.
6 C. Zhou, B. Yuan, S. Zhang, X. Yang and J. Zhong, *Chem. Ind. Eng. Prog.*, 2019, **38**, 4614–4622.
7 M. Taddei, *Coord. Chem. Rev.*, 2017, **343**, 1–24.
8 M. C. de Koning, M. van Grol and T. Breijaert, *Inorg. Chem.*, 2017, **56**, 11804–11809.
9 J. M. Palomba, C. V. Credille, M. Kalaj, J. B. DeCoste, G. W. Peterson, T. M. Tovar and S. M. Cohen, *Chem. Commun.*, 2018, **54**, 5768–5771.
10 S. G. Ryu, M.-K. Kim, M. Park, S. O. Jang, S. H. Kim and H. Jung, *Microporous Mesoporous Mater.*, 2019, **274**, 9–16.
11 B. Bueken, N. Van Velthoven, T. Willhammar, T. Stassin, I. Stassen, D. A. Keen, G. V. Baron, J. F. M. Denayer, R. Ameloot, S. Bals, D. De Vos and T. D. Bennett, *Chem. Sci.*, 2017, **8**, 3939–3948.
12 T. Tian, Z. Zeng, D. Vulpe, M. E. Casco, G. Divitini, P. A. Midgley, J. Silvestre-Albero, J. C. Tan, P. Z. Moghadam and D. Fairen-Jimenez, *Nat. Mater.*, 2018, **17**, 174–179.
13 S. M. F. Vilela, P. Salcedo-Abraira, L. Micheron, E. L. Solla, P. G. Yot and P. Horcajada, *Chem. Commun.*, 2018, **54**, 13088–13091.
14 W. Cui, X. Kang, X. Zhang and X. Cui, *J. Phys. Chem. Solids*, 2019, **134**, 165–175.
15 J. Hou, A. F. Sapnik and T. D. Bennett, *Chem. Sci.*, 2020, **11**, 310–323.
16 D. B. Dwyer, N. Dugan, N. Hoffman, D. J. Cooke, M. G. Hall, T. M. Tovar, W. E. Bernier, J. DeCoste, N. L. Pomerantz and W. E. Jones, Jr, *ACS Appl. Mater. Interfaces*, 2018, **10**, 34585–34591.
17 H. Liang, A. Yao, X. Jiao, C. Li and D. Chen, *ACS Appl. Mater. Interfaces*, 2018, **10**, 20396–20403.
18 D. L. McCarthy, J. Liu, D. B. Dwyer, J. L. Troiano, S. M. Boyer, J. B. DeCoste, W. E. Bernier and W. E. Jones, Jr, *New J. Chem.*, 2017, **41**, 8748–8753.
19 Y. Hara, K. Kanamori and K. Nakanishi, *Angew. Chem., Int. Ed.*, 2019, **58**, 19047–19053.
20 Y. Dong, L. Cao, J. Li, Y. Yang and J. Wang, *RSC Adv.*, 2018, **8**, 32358–32367.
21 J. Zhao, L. Xu, Y. Su, H. Yu, H. Liu, S. Qian, W. Zheng and Y. Zhao, *J. Environ. Sci.*, 2021, **101**, 177–188.
22 L. Wen, X. Chen, C. Chen, R. Yang, M. Gong, Y. Zhang and Q. Fu, *Arabian J. Chem.*, 2020, **13**, 5669–5678.
23 D. Xie, Y. Gu, H. Wang, Y. Wang, W. Qin, G. Wang, H. Zhang and Y. Zhang, *J. Colloid Interface Sci.*, 2019, **542**, 269–280.
24 Y. Khabzina, J. Dhainaut, M. Ahlhelm, H. J. Richter, H. Reinsch, N. Stock and D. Farrusseng, *Ind. Eng. Chem. Res.*, 2018, **57**, 8200–8208.
25 L. R. Redfern, L. Robison, M. C. Wasson, S. Goswami, J. Lyu, T. Islamoglu, K. W. Chapman and O. K. Farha, *J. Am. Chem. Soc.*, 2019, **141**, 4365–4371.
26 D. W. Lee, T. Didriksen, U. Olsbye, R. Blom and C. A. Grande, *Sep. Purif. Technol.*, 2020, **235**, 116182–116193.
27 L. Li, S. Xiang, S. Cao, J. Zhang, G. Ouyang, L. Chen and C. Y. Su, *Nat. Commun.*, 2013, **4**, 1774–1782.
28 A. Carne-Sanchez, G. A. Craig, P. Larpent, T. Hirose, M. Higuchi, S. Kitagawa, K. Matsuda, K. Urayama and S. Furukawa, *Nat. Commun.*, 2018, **9**, 2506–2513.
29 J. Santos-Lorenzo, R. San José-Velado, J. Albo, G. Beobide, P. Castaño, O. Castillo, A. Luque and S. Pérez-Yáñez, *Microporous Mesoporous Mater.*, 2019, **284**, 128–132.
30 X. Zhang, Y. Yang, L. Song, J. Chen, Y. Yang and Y. Wang, *J. Hazard. Mater.*, 2019, **365**, 597–605.
31 C. Yin, Q. Liu, R. Chen, J. Liu, J. Yu, D. Song and J. Wang, *Ind. Eng. Chem. Res.*, 2019, **58**, 1159–1166.
32 H. Wu, Y. S. Chua, V. Krungleviciute, M. Tyagi, P. Chen, T. Yildirim and W. Zhou, *J. Am. Chem. Soc.*, 2013, **135**, 10525–10532.
33 M. J. Katz, Z. J. Brown, Y. J. Colon, P. W. Siu, K. A. Scheidt, R. Q. Snurr, J. T. Hupp and O. K. Farha, *Chem. Commun.*, 2013, **49**, 9449–9451.
34 J. Ren, H. W. Langmi, B. C. North, M. Mathe and D. Bessarabov, *Int. J. Hydrogen Energy*, 2014, **39**, 890–895.